Bulletin of the Seismological Society of America, Vol. 105, No. 3, pp. 1739–1755, June 2015, doi: 10.1785/0120140261

Engineering Implications of Source Parameters and 3D Wave Propagation Modeling for the 2004 Parkfield, California, Earthquake

by Karin Şeşetyan, Eser Çaktı, and Raul Madariaga

Abstract The 2004 M_w 6.0 Parkfield, California, earthquake took place in a very well-instrumented area, producing a substantial quantity of high-quality near-field recordings. Taking advantage of the rare luxury of having a large number of near-field ground-motion recordings distributed around the fault zone and the availability of various slip models as well as an Earth structure model of the region, we study the effects of various kinematic rupture parameters to derive implications for strong ground motion simulation in engineering applications. We model the 3D wave propagation resulting from this earthquake using the 3D staggered-grid finite-difference method. Using a grid spacing of 100 m in our fourth-order explicit finite-difference code, we could properly resolve frequencies of up to 1 Hz with a minimum of eight grids per wavelength for shear waves, except in the immediate vicinity of the fault where fault-trapped waves dominate the records. We assess the effects of various simulation parameters such as slip model, rise time (constant or variable), rupture velocity, and the earth model (1D versus 3D) on the resulting waveforms. We also investigate the distribution of engineering parameters such as peak ground velocities, peak ground displacements, and spectral accelerations at specific periods on the Earth's surface. An outstanding feature is that at high frequencies fault-normal components near the edge of fault segments dominate the ground-motion field. Fault-parallel components are dominated by lower frequencies. The difference between fault-parallel and fault-normal components is clearly observed in such engineering parameters as peak ground velocity and peak ground displacement.

Introduction

The Parkfield, California, segment of the San Andreas fault generated moderate-size earthquakes in 1881, 1901, 1922, 1934, and 1966 that were tentatively interpreted as characteristic earthquakes with a return period of approximately 25 years (Bakun and McEvilly, 1979; Bakun and Lindh, 1985; Bakun *et al.*, 2005). Because of the high probability of return of a characteristic earthquake on this segment, the Parkfield area was densely instrumented by the California Strong Motion Instrumentation Program (CSMIP) and U.S. Geological Survey (USGS). The expected earthquake occurred on September 2004, with a moment magnitude of 6.0. The hypocenter was 11 km southeast of Parkfield (epicenter at 35.825° N, 120.374° W) at a depth of 8 km. Analyses conducted by the USGS and the University of California at Berkeley (UCB) revealed that the event had a strike-slip mechanism, with strike and dip angles of 140° and 87°, respectively. Analysis of the aftershocks and rupture models indicates that the fault ruptured along the same section of the fault as that of the previous events in the similar magnitude Parkfield earthquake series. However, unlike the 1922, 1934, and 1966 shocks, which ruptured from northwest to southeast, the 2004 earthquake initiated in the southeast and ruptured to the northwest.

The 2004 Parkfield earthquake produced one of the best near-field datasets ever recorded, with 56 recordings within 20 km of the fault trace (Shakal *et al.*, 2005; Fig. 1). The configuration of the array run by the California Geological Survey (CGS) consisted of a group of analog strong ground motion stations installed parallel to the fault (called fault zone stations), complemented by three lines of stations (the Cholame, Gold Hill, and Vineyard Canyon limbs), extending perpendicularly from the fault. In addition to these three limbs, the shorter Stone Corral limb extended to the east (McJunkin and Shakal, 1983). The strong-motion data recorded by the CGS array were critically analyzed by Shakal *et al.* (2006). The Parkfield strong-motion instrumentation also included 12 high-resolution General Earthquake Observation System (GEOS) recorders installed by the USGS. The analysis results of these recordings were presented in Borcherdt *et al.* (2006).

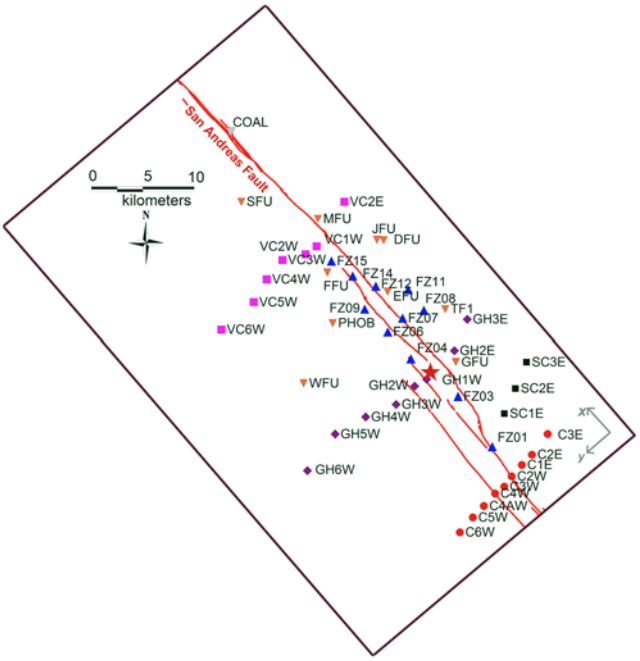

Figure 1. The 2004 Parkfield earthquake and the distribution of near-field stations. The star indicates the location of the epicenter. Station labels beginning with C form the Cholame array; SC, the Stone Corral array; GH, the Gold Hill array; FZ, the fault zone array; and VC, the Vineyard Canyon array of the California Strong Motion Instrumentation Program (CSMIP). COAL is the Coalinga Slack Canyon station. The remaining stations are those run by the U.S. Geological Survey. The rectangle represents the top view of the simulation cube. The x axis is set parallel to the surface projection of the fault. Strike and dip angles of the rupture plane are 140° and 87°, respectively. The color version of this figure is available only in the electronic edition.

Several kinematic studies of the rupture process of the 2004 Parkfield earthquake were carried out by Ji (2004; see Data and Resources), Dreger *et al.* (2005), Ji *et al.* (2004), Liu *et al.* (2006), and Ma *et al.* (2008). Dynamic inversions were proposed by Ma *et al.* (2008) and Twardzik *et al.* (2014). Twardzik *et al.* (2012) studied the resolution of kinematic inversions at low frequencies, reaching the conclusion that the most robust feature of the rupture process is the presence of two elongated quasihorizontal slip patches at depths between 5 and 10 km.

Although the Parkfield earthquake presents the researcher with all types of readily available input information for simulation (a 3D velocity model, various slip models, and an excellent set of recordings), such attempts have been limited. Mena *et al.* (2006) simulated the Parkfield earthquake recordings by hybrid Green's functions technique. Gallovič *et al.* (2010) simulated the recordings at extreme near field (stations of the fault zone array and stations of remaining arrays positioned practically above the fault rupture) with the goal of investigating the effect of fault geometry, velocity model, and topography on resulting particle motions. In this article, we present a 3D simulation of the Parkfield earthquake strong-motion data set using the 3D velocity model of Thurber *et al.* (2006) and the kinematic slip models of Ji (2004; see Data and Resources), Ji *et al.* (2004), Dreger *et al.* (2005), and Liu *et al.* (2006). We discuss our results from the point of view of assessing the performance of our simulation technique and our selection of various slip models by station-based comparisons. Thereafter, we turn our attention to the estimation of several engineering parameters of the Parkfield earthquake using the simulation results from our dense, spatially homogeneous simulation grid.

Simulation of the 3D Wavefield

Methodology

Finite differences are well established as a suitable tool to simulate wave propagation in the vicinity of seismic sources in heterogeneous media. Several applications of the method have been proposed in the seismological literature (e.g., Miyatake, 1980; Graves, 1996; Olsen and Archuleta, 1996; Pitarka and Irikura, 1996; Moczo *et al.*, 2014).

The staggered-grid velocity-stress finite-difference method used in the present study was originally proposed by Madariaga (1976) to study seismic quasidynamic rupture propagation in a homogeneous, isotropic, elastic media. The method was extended to heterogeneous media by Virieux (1986) and brought to fourth-order accuracy in space by Levander (1988). Olsen *et al.* (1995) and Olsen and Archuleta (1996) used the fourth-order staggered grid method to study large-scale kinematic simulations of wave propagation in the Los Angeles area. Madariaga *et al.* (1998) extended the fourth-order staggered-grid finite-difference method to study dynamic faulting in 3D. For a full description of the method, we refer to Madariaga *et al.* (1998) and Moczo *et al.* (2014). Here we discuss only the foundations of the method. We solve the following system of first-order partial differential equations:

$$\rho \frac{\partial v_i}{\partial t} = \frac{\partial \sigma_{ij}}{\partial x_j} \tag{1a}$$

and

$$\frac{\partial \sigma_{ij}}{\partial t} = \lambda \frac{\partial v_i}{\partial x_i}\delta_{ij} + \mu\left(\frac{\partial v_i}{\partial x_j} + \frac{\partial v_j}{\partial x_i}\right) + \dot{M}_{ij}, \tag{1b}$$

in which v_i are the velocity components, σ_{ij} are the stress components, λ and μ are the elastic constants of the medium, and $M(x,t)$ is the seismic moment tensor distribution. $\dot{M}$ means the time derivative or moment rate. We observe that the source in this equation is the moment rate distribution that we represent in the simplified form

$$\dot{M}_{ij}(x,t) = \mu(x)D(x)s(t), \tag{2}$$

in which μ is the local rigidity, $D(x)$ is the slip distribution, and $s(t)$ is the source time function that we will define below. In our simulations, both μ and D are variable on the fault, but $s(t)$ will be assumed to be the same for every point in the

fault. The rupture velocity v, implicit in the space dependence of $s(t)$, may be variable (as discussed later in the text). The slip distributions inverted by different authors used different grid spacing. These slip distributions were interpolated to obtain the same grid spacing as in the numerical model maintaining the same spatial resolution as in the original models. The fault in our simulations is not vertical, so it does not coincide with one of the grid planes of the finite-difference grid. The moment tensor source was applied to the closest node from the fault; this poses an obvious problem when the rigidity is different on the two sides of the fault. This can be improved by smoothing the moment tensor distribution over several grid points; however, because we consistently used eight nodes per wavelength, we did not observe much change when the moment tensor density was distributed on several nodes (the thick fault approach of Madariaga *et al.*, 1998).

We used the same source time function $s(t)$ at each element of the fault. We studied several types of source time functions in the numerical simulations, including a trapezoidal and an exponentially decreasing source function (Brune, 1970)

$$s(t) = Ate^{-\kappa t}, \tag{3}$$

in which A is the amplitude and κ determines the duration and rise time of the source time function. The frequency content of the signal in equation (3) is determined by the corner frequency (κ) of the signal. In all the simulations presented in this article, we used the exponential source time function because the shape of $s(t)$ does not significantly affect the waveforms.

Frequency resolution is one of the main problems with deterministic ground-motion simulation methods. Two conditions must be imposed on the choice of grid spacing Δh and time interval Δt, which are both related to the velocity structure. The first condition is that the finite-difference simulation must satisfy the so-called Courant–Friedrichs–Lewy (CFL) parameter, defined as $H = v_P \Delta t / \Delta h$, in which v_P is the largest value of the P wave of the medium (Courant *et al.*, 1928; Madariaga, 1976). In all the numerical models of the present study H is close to 0.3. The second condition was that the frequency resolution of the simulation is governed by the number of nodes per minimum shear wavelength propagated in the model. The frequency content of the slip model should be chosen so that the maximum frequency propagated by the grid has a shear wavelength that is longer than eight grid steps.

Model Parameters

The modeled region in the source area of the Parkfield earthquake extends 55 km in the northwest–southeast direction parallel to the fault and 33 km in the northeast–southwest direction normal to the fault. The depth of the model is 18 km. A grid spacing of 100 m and a time step of 0.004 s are used. With a maximum P-wave velocity of 7000 m/s used in the modeling of the Earth structure, the typical value of the CFL parameter is 0.28. The 3D velocity wavefield is generated for a rectangular prism of $550 \times 330 \times 180$ nodes in fault parallel (FP), fault normal (FN), and vertical directions, respectively. With a grid size of 100 m, we estimate that we can simulate seismic-wave propagation for wavelengths longer than 800 m that is slightly less than 1 Hz for shear wavespeeds of the order of 1000 m in the shallower layers of our velocity models.

Modal Bias

Time histories are compared with real data obtained from 48 stations located around the fault (Fig. 1). The modal bias between the observed and simulated ground velocities, calculated by the ratio of their smoothed Fourier amplitude spectra averaged over the 48 stations is used as an indicator of the goodness of fit. The modal bias is a good indicator from the engineering point of view because it provides information over the frequency range of interest, which in our case is the frequency band of the simulations. The modal bias is calculated as

$$B(f) = \frac{1}{n} \sum_{i=1}^{n} \log\left(\frac{O_i(f)}{S_i(f)}\right), \tag{4}$$

in which $O_i(f)$ and $S_i(f)$ are the observed and simulated amplitude spectra, respectively, and n is the number of stations for which the data are compared.

Slip model, rupture velocity, rise time of the source time function, and crustal velocity structure are the kinematic simulation parameters that we choose to study. In the following, we describe each parameter and discuss the effect that their variation caused in simulation results using the modal bias as a measure.

Slip Model

Numerical wave propagation simulations were conducted for four slip models that have been proposed for the 2004 Parkfield earthquake. These were the preliminary slip model developed by Ji (2004; see Data and Resources), the rapid finite-source model of Dreger *et al.* (2005), the slip model of Ji *et al.* (2004), which was obtained from data of 14 strong-motion and 13 Global Positioning Systems stations, and the slip model of Liu *et al.* (2006), which was based on the kinematic inversion of recordings of 43 near-field stations. A summary of the parameters related to different source models is presented in Table 1. All models (Fig. 2) were based on low-pass-filtered data at 1 Hz. As shown in Figure 3, we found that the preliminary models proposed by Ji (2004; see Data and Resources) and Dreger *et al.* (2005) had a larger modal bias than the other two. The modal biases were significantly reduced for the slip model of Ji *et al.* (2004) and Liu *et al.* (2006); we retained these models for

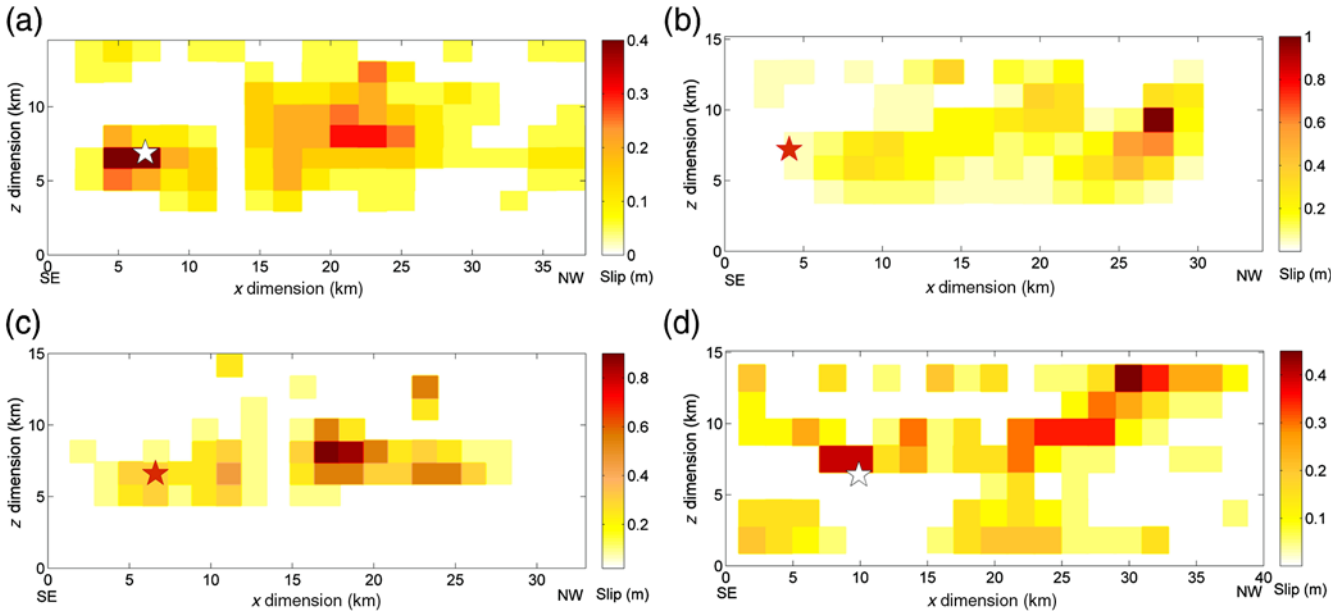

Figure 2. Slip models of 2004 Parkfield earthquake proposed in various kinematic studies: (a) Ji (2004; see Data and Resources), (b) Dreger *et al.* (2005), (c) Ji *et al.* (2004), and (d) Liu *et al.* (2006). The color version of this figure is available only in the electronic edition.

more detailed study. It is important to remark that the variation of other kinematic rupture parameters such as rupture velocity, rise time, and the local soil conditions as indicated in Liu *et al.* (2006) will also affect the modal biases, as explained in the following sections.

Rupture Velocity

The average rupture velocities proposed in the individual slip models are incorporated in the study. The average rupture velocity suggested by Liu *et al.* (2006) is 2.8 km/s, which is the value used in our simulations. However, Liu *et al.* (2006) also proposed two zones with distinctly different average rupture velocities. The first zone was located around the hypocenter with an average rupture velocity of 2.8 km/s, and the second zone had an average rupture velocity V_r of 3.3 km/s in the secondary region of large slip to the northwest of the hypocenter. These two zones are incorporated in the source model, and the results are compared for different rise-time values. As shown in Figure 4, where we compare the modal bias for the different models, the variable V_r models with a lower rise-time value improved the simulation at higher frequencies.

Rise Time

Based on the slip model of Liu *et al.* (2006) and the exponential source time function, we tried several rise-time values (κ) to understand its effect on the frequency content of the simulations. Two approaches were used: the first imposed the same rise-time value (κ) for all the grids on the fault surface, and the second used the rise-time values proposed in the original kinematic models. The comparison of the modal bias thus obtained shows that although a very stable simulation of the wavefield is obtained for constant rise-time values above 0.8 s, larger disturbances of the wavefield were observed for a rise time of 0.4 s. Nevertheless a lower modal bias is obtained for a rise time of 0.4 s which is the lowest value that

Table 1
Parameters Related to Different Source Models of the 2004 Parkfield Earthquake

Source Model	M_w	Strike (°)	Dip (°)	Rake (°)	Length (km)	Width (km)	Dx (km)*	Dz (km)*	Average Rise Time (s)	Average Rupture Speed (km/s)	$F_{min} - F_{max}$ (Hz)
Ji (2004; see Data and Resources)	5.90	137	83	181	40.00	14.50	2.00	1.45	—	—	–
Dreger *et al.* (2005)	6.0	137	80	180	34.00	15.50	1.89	1.72	—	3.20	0.01–1.00
Ji *et al.* (2004)	—	141	—	150–210	33.00	15.00	1.50	1.50	—	2.85	—
Liu *et al.* (2006)	6.06	140	87	141	40.00	15.00	1.90	1.70	0.88	2.80	0.01–1.00

*Dx and Dz are the grid sizes of the original source models along strike and dip directions, respectively.

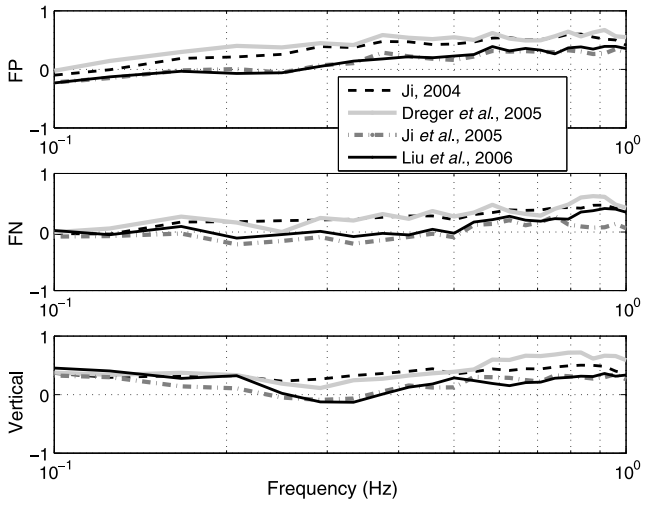

Figure 3. Modal bias of observed/simulated velocities, computed for the various slip models proposed for the Parkfield earthquake of 2004. FP and FN represent the fault-parallel and fault-normal components, respectively. The slip models are defined in Figure 2.

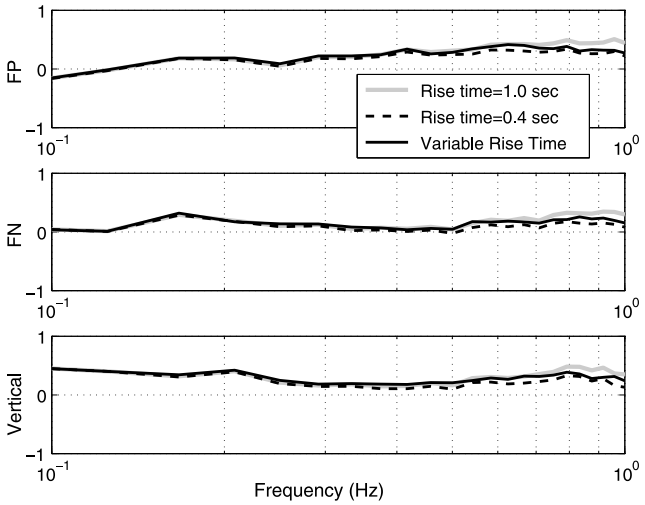

Figure 5. Modal bias of observed/simulated velocities, obtained from various rise times of the exponential source time function compared with a model with variable rise time from Liu *et al.* (2006).

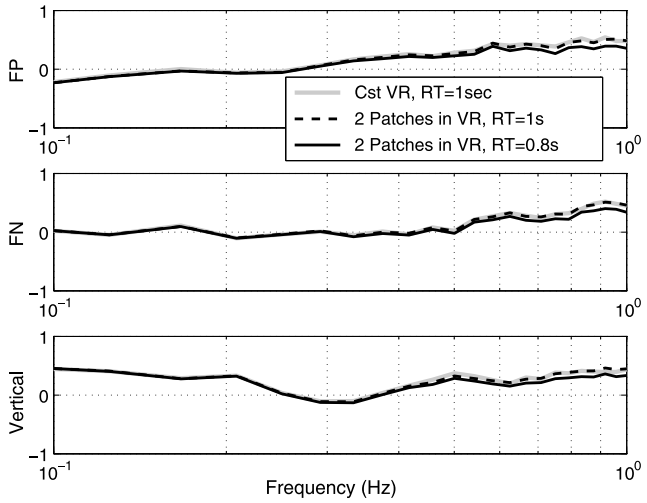

Figure 4. Modal bias of observed/simulated velocities, obtained from various rupture velocity models discussed in the text. VR is rupture velocity, and RT is rise time.

can be used with our finite-difference grid. For shorter values of the rise-time, simulations become very noisy. As shown in Figure 5, variable rise time did not improve the results, as the values ranged from 0.4 to 4.0 s.

Crustal Velocity Model

The geologic structure in the Parkfield region is very complex east of the fault where mostly Mesozoic sedimentary and metamorphic rocks are exposed. To the west of the fault, less structurally deformed sedimentary deposits of middle-to-late Cenozoic age, cover older and more structurally complex Mesozoic terrain of the Salinian block (McJunkin and Shakal, 1983). The initial velocity structure used in the analysis was adopted from the velocity model provided by the USGS. To be compatible with the grid size used in the 3D finite-difference simulation and also with the frequency resolution aimed for ($f_{\max} = 1$ Hz), the lowest shear-wave velocity was taken as 1000 m/s. Depending on the availability of information and on the suitability of the model for the inversion method used, different but comparable crustal velocity models have been used in the derivation of the slip models for the 2004 Parkfield earthquake. Ji *et al.* (2004) and Liu *et al.* (2006) used different 1D velocity models for the southwest and northeast sides of the fault. The 3D velocity model of the Parkfield region became available in 2006 (Thurber *et al.*, 2006). In the present study, the velocity structures used in individual studies were adopted, but the results were also compared with those obtained using the 3D velocity structure. The 3D shear-wave velocity and density models were derived from the compressional-wave velocity model provided in Thurber *et al.* (2006) using the empirical conversion equations by Brocher (2005). One-dimensional velocity structures differentiated for the northeast and southwest sides of the fault, as used in Ji *et al.* (2004) and Liu *et al.* (2006), are shown in Figure 6. In Figure 7, we present an FN cross section of the *P*-wave velocity structure obtained from the data presented in Thurber *et al.* (2006). In Figure 8, we show the modal bias for the kinematic models proposed by Ji *et al.* (2004) and Liu *et al.* (2006), both for a two-sided 1D velocity model and for the Thurber *et al.* (2006) 3D model.

Local Site Effects

As an approximation to site effects, Liu *et al.* (2006) used the data recorded by the Parkfield array during the

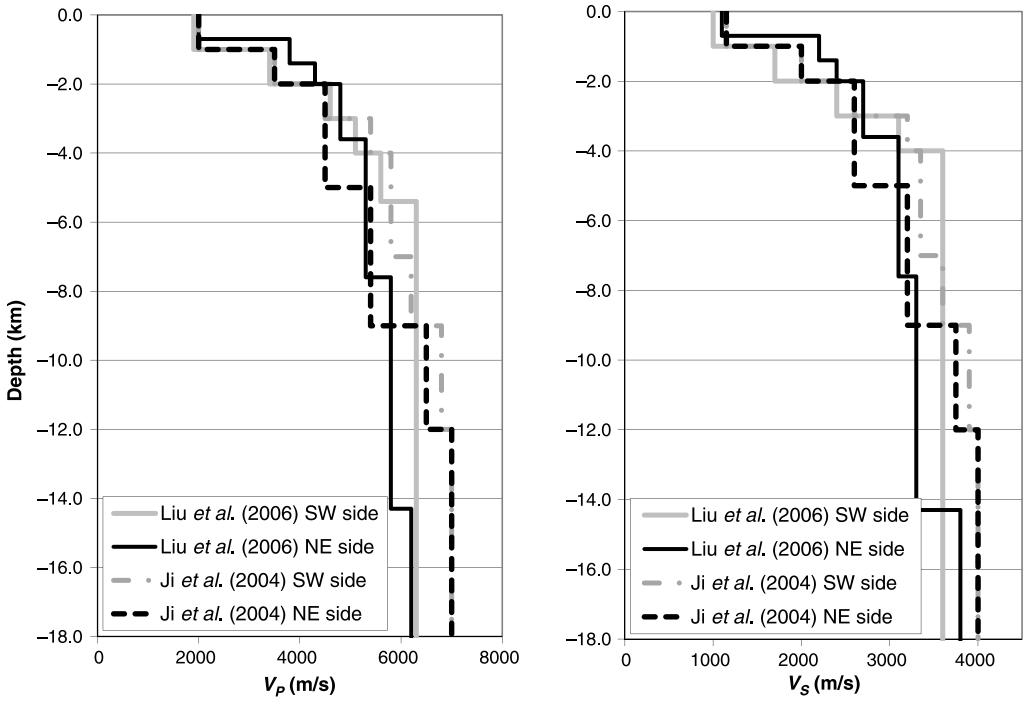

Figure 6. 1D velocity structures on either side of the San Andreas fault near Parkfield used by different authors in the kinematic inversions. Differences in shear wavespeed on the two sides of the fault affect numerical simulations by finite differences.

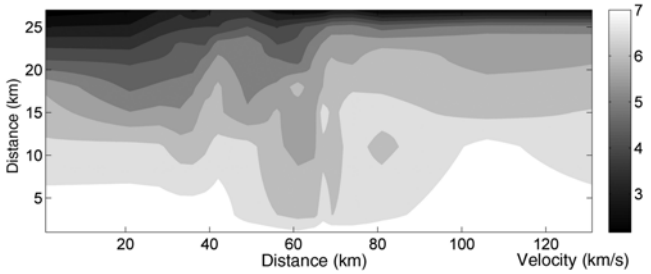

Figure 7. Fault-normal cross section of the *P*-wave velocity structure at $Y = -21$ km (northwest side of the epicenter) for the Thurber *et al.* (2006) model of the *P*-wave structure in the Parkfield area (cross section in northeast–southwest direction).

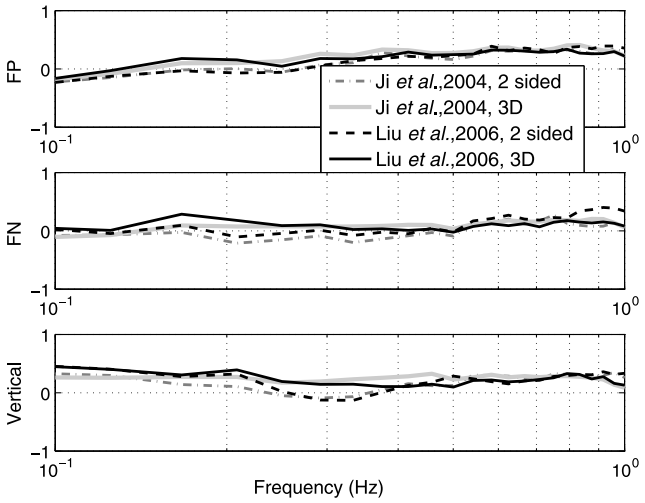

Figure 8. Modal bias of observed/simulated velocities, obtained using two-sided 1D and 3D velocity structures.

1983 M_w 6.5 Coalinga earthquake. Assuming the source is common to all stations, the deviation from a reference source spectrum is taken as a measure of the site effect. Using this method, constant coefficients of site amplification were obtained for the frequency range of interest (0.16–1 Hz). To remove the local site effect at the station level, the recorded data during the 2004 Parkfield earthquake were divided by these coefficients. When the same coefficients are used in the calculation of modal bias for both the two-sided 1D and the 3D velocity structures, the bias was significantly reduced (Fig. 9).

Simulation results, especially on the FP component are generally more successful for the stations located on the northeastern side of the fault than those on the southwestern side, as shown in Figure 10. This result may be affected by the use of moment rate (see equation 2) as a source in the finite-difference code. Because the slip models by the different authors were defined in terms of slip and slip rate on the fault, we had to compute the seismic moment rate (equation 2), taking into account the value of rigidity of the 3D model on either side of the fault. Thus, the apparent moment tensor is larger, as seen by the northeastern stations. The only way to fully resolve this ambiguity in the definition of

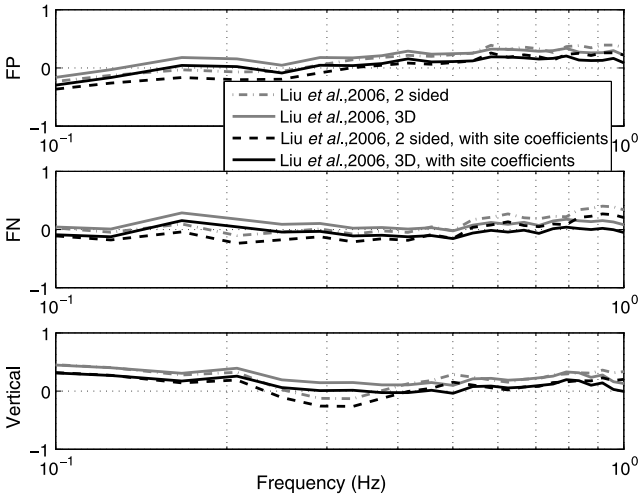

Figure 9. Modal bias of observed/simulated velocities, obtained using the two-sided 1D and 3D velocity structures with site coefficients suggested in Liu *et al.* (2006).

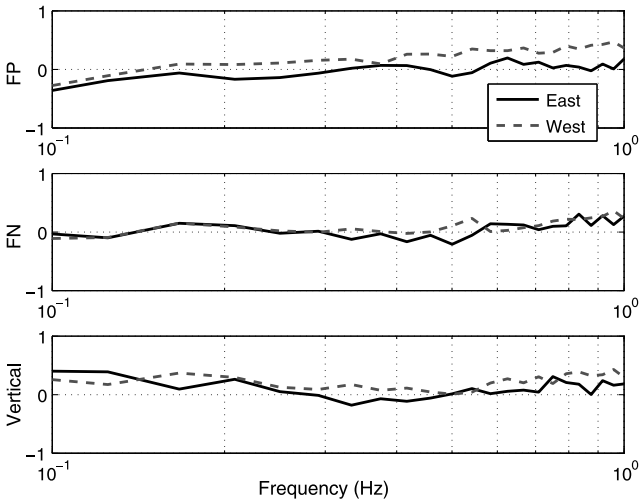

Figure 10. Modal bias of observed/simulated velocities for stations on the eastern and western sides of the fault, using simulations obtained from the 3D velocity structure. The difference in amplitude between the northeastern and southwestern sides of the fault is affected by the rigidity used in the definition of seismic moment (equation 2).

moment tensor would be to use a finite-difference code for the kinematic inversion, but this is well beyond the purpose of the present article.

Comparison of Synthetics with Recorded Data

In this section, we present an array-based comparison and evaluation of the simulated and recorded velocity time histories. The recorded strong ground motion data set of the 2004 Parkfield earthquake was obtained from COSMOS Virtual Data Center (see Data and Resources). The results obtained from the slip model of Liu *et al.* (2006) using the 3D velocity structure of the Parkfield region and incorporating (when available) the site amplification factors given in Liu *et al.* (2006) are used for the comparison (Fig. 11). All recorded and simulated time histories are low-pass filtered at 1 Hz, which is the maximum frequency that can be modeled with a grid of 100 m and a minimum shear wavespeed of 1000 m. It should be noted that the fit in the vertical component of the ground motion is generally poorer than the horizontal components, because Liu *et al.* (2006) assigned only 10% weight to the vertical components of the recordings during the inversion process. In spite of this weighting, the goodness of fit of the vertical components is also satisfactory except for the Cholame array, which lies in the backward directivity zone and the fault zone array, which produced the worst overall results because of the waves trapped in the fault zone.

Gold Hill Array

The Gold Hill array is approximately perpendicular to the fault and passes through the epicenter. The ground motion recorded by this array is particularly sensitive to the initial part of the rupture and does not show directivity effects. Velocity and displacement amplitudes of this array in the FP direction are larger than those in the FN direction.

Stone Corral Array

The Stone Corral array consists of three instruments located in the northeast side of the fault close to the southwestern end of the rupture and at an angle slightly less than 90° with respect to the fault plane. The closest station is at a distance of about 3 km to the fault. The goodness of fit for this array is generally satisfactory for all components.

Vineyard Canyon Array

The Vineyard Canyon array is approximately perpendicular to the fault plane and is located at a 15 km distance from the epicenter in the forward directivity region close to the northern end of the rupture. The amplitudes in the FN direction are generally larger than those in the FP direction and are consistently larger than those in the Gold Hill array, a behavior observed in both recordings and simulations and which is consistent with the expected directivity effects. As in the Gold Hill array, the goodness of fit of the station closest to the fault is less satisfactory than those in the mid-distance range of the array.

Cholame Array

The Cholame array is also perpendicular to the fault close to the southeastern end of the rupture. Like the Vineyard Canyon array, the Cholame array exhibits forward directivity characteristics with FN components larger than FP components.

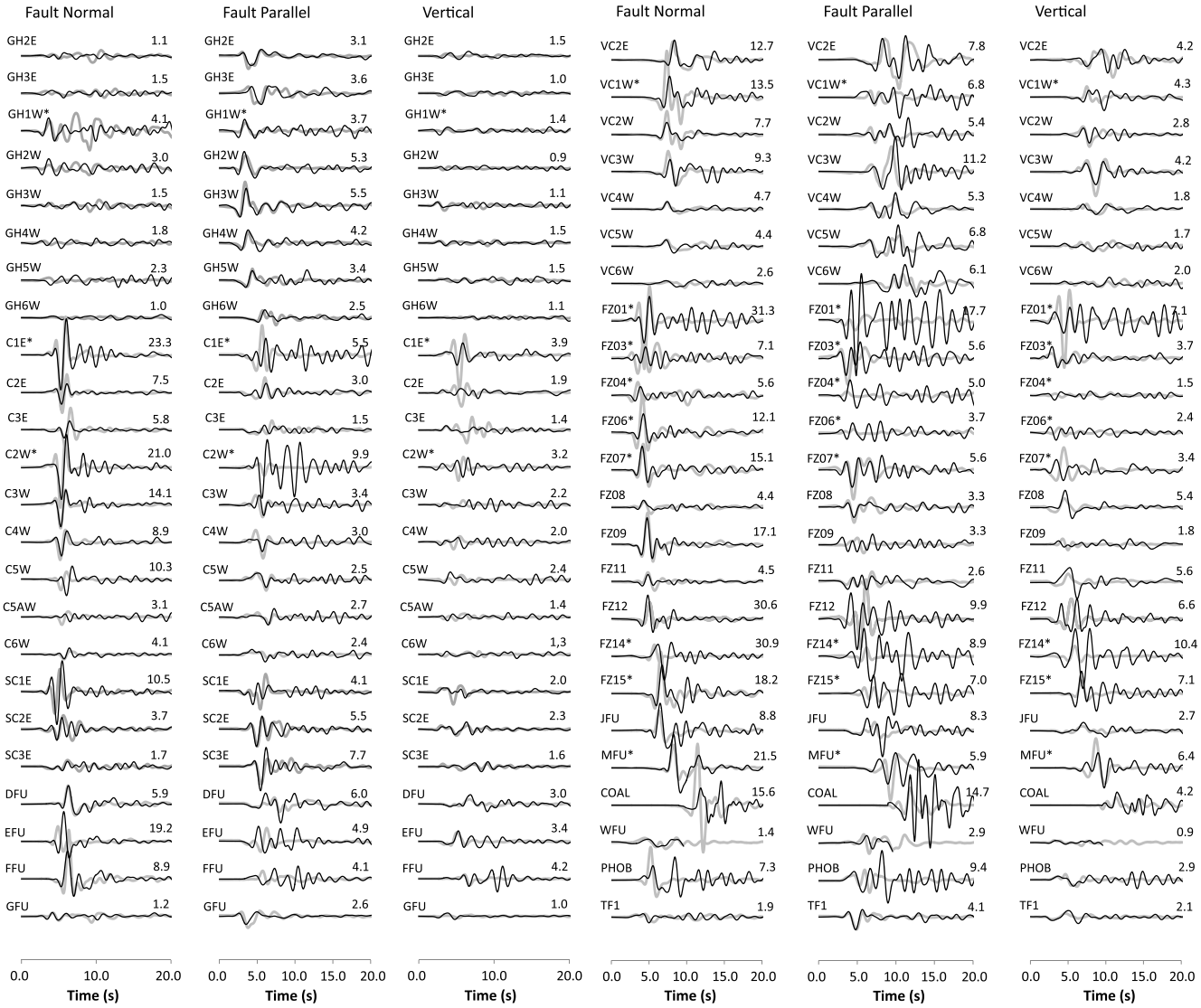

Figure 11. Comparison between recorded (black) and simulated (gray) velocity waveforms for the preferred slip model. The components of motion shown are fault normal, fault parallel, and vertical. The codes of the stations are indicated at the left side, whereas the recorded peak velocities (in cm/s) are indicated on the right side of each subplot. The waveforms are plotted for duration of 20 s. All recorded and simulated time histories are low-pass filtered at 1 Hz. The recordings in the immediate vicinity of the fault are indicated with asterisks, following the discussion by Gallovič *et al.* (2010).

USGS Array

The USGS array consists of nine instruments distributed in the near-fault region. Among those stations, the fit is particularly satisfactory at station TF1, which is known to be located on rock, and the recording was not used in the inversion process by Liu *et al.* (2006).

Fault Zone Array

The fault zone array was deployed in order to study the variation of strong ground motion along the fault. Because all stations along the fault zone array are located very close to the fault, the goodness of fit of the simulated and recorded time histories is less satisfactory; the reason is that in the immediate vicinity of the fault, the records are dominated by the fault-trapped waves. The same problem is also observed at the stations of the fault perpendicular arrays located at the immediate vicinity of the fault. However, stations of the fault zone array, which are located at a distance larger than a few kilometers of the fault, produced much better results (e.g., FZ01 versus FZ08 in Fig. 11). In general, the fit of the FN component in the near-fault stations is better than the FP component. Gallovič *et al.* (2010) found that among fault geometry, topography, and velocity structure (1D versus 3D), the heterogeneous 3D velocity structure produces the best-fitting simulated velocities to recordings in the extreme near field. This conclusion is based on the simulation of extreme near-field stations only. In Figure 11, the

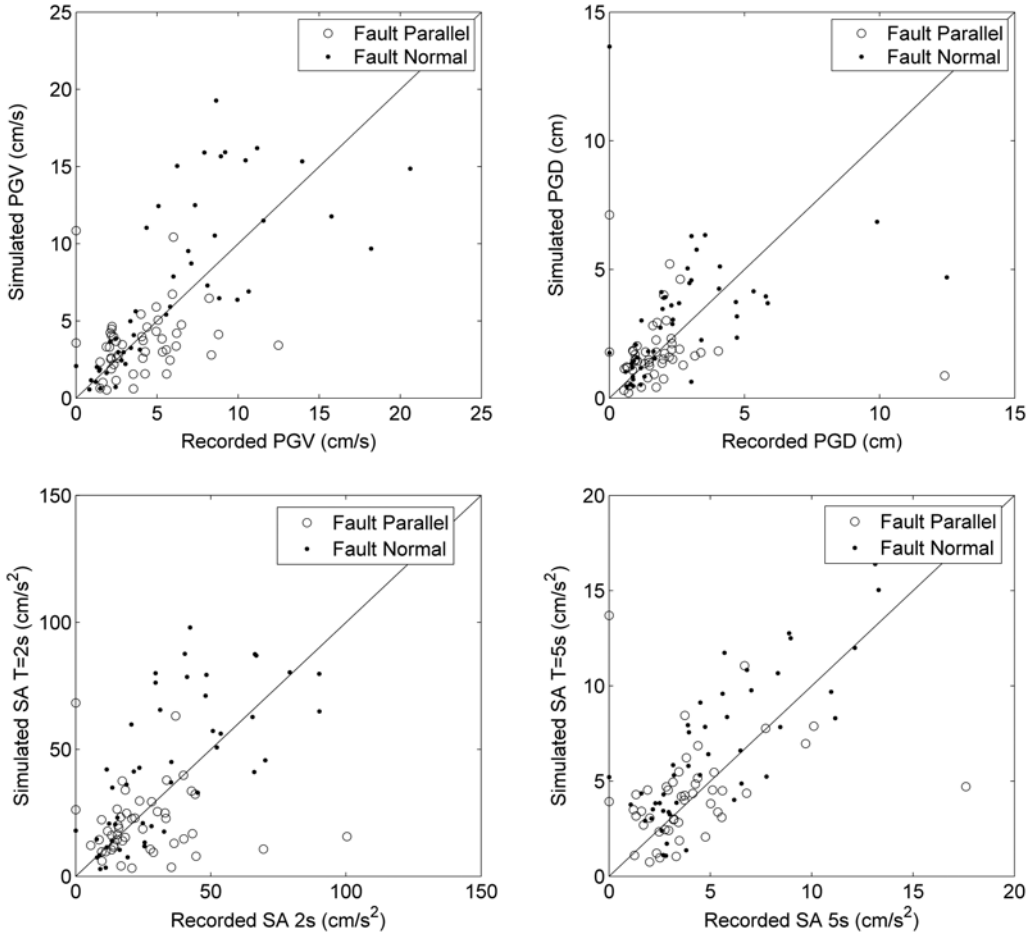

Figure 12. Comparison of simulated and recorded peak ground velocities (PGVs), peak ground displacements (PGDs), and spectral accelerations (SAs) ($T = 2.0$ and 5.0 s). Recorded ground motions are filtered between 0.1 and 1.0 Hz and corrected for engineering bedrock conditions to enable a comparison with simulations. Site correction is carried out using the coefficients provided by Liu *et al.* (2006).

stations used by Gallovič *et al.* (2010) are marked with an asterisk. Although we use a 3D velocity model and simulate the velocities at almost all stations in the Parkfield region, the poorest fit is still associated with the extreme near-field stations. This suggests that the misfit must be related to other phenomena, possibly to fault-trapped waves.

Simulated Versus Recorded Peak Ground Velocities and Peak Ground Displacements

In Figure 12, we present the comparison of recorded and simulated peak ground velocities (PGVs) and peak ground displacements (PGDs), both filtered between 0.1 and 1.0 Hz. For recorded FN PGVs less than about 6 cm/s, we observe a very good fit between recorded and simulated velocities. The fit between recorded and simulated FP components in the same velocity range is also very good, although we should note that for velocities larger than 6 cm/s, FP PGVs are overestimated by the simulations; the overestimation is never larger than a factor of 2. There is a very reasonable fit between recorded and simulated PGDs in FP and FN directions, which is in general better than the fit of PGVs. We also compare simulated and recorded spectral accelerations (SAs) at 2.0 and 5.0 s periods in the same figure. For $T = 5.0$ s SAs, there is almost a perfect match between the SAs for both FP and FN components. For $T = 2.0$ s SAs, the spread around the 45° line is almost symmetrical for the case of FP components. FN components are slightly overestimated by a factor that is is always less than 2.

Analysis of Engineering Parameters

In this section, based on our preferred slip model (Liu *et al.*, 2006), we analyze the spatial distribution of various ground-motion parameters obtained for the entire simulation surface and explore in what way the kinematically simulated ground motions can be used in engineering applications and to what extent the simulated ground motion can compensate for the lack of recorded data. Before entering this discussion, we present in Figure 13 the surface distribution of PGVs obtained from interpolation of recorded and simulated values at station locations only. We observe a striking similarity between the two PGV distributions. Next, the ground surface distribution of synthetic PGVs and PGDs, as obtained from

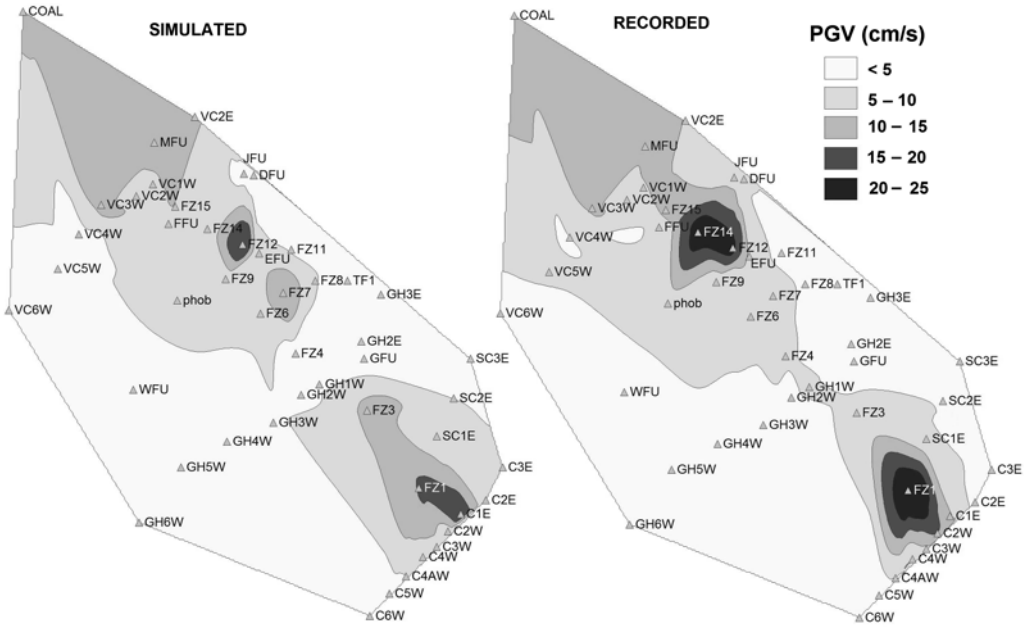

Figure 13. Comparison of (left) simulated and (right) recorded PGV (geometric mean) contours obtained from interpolation of station data.

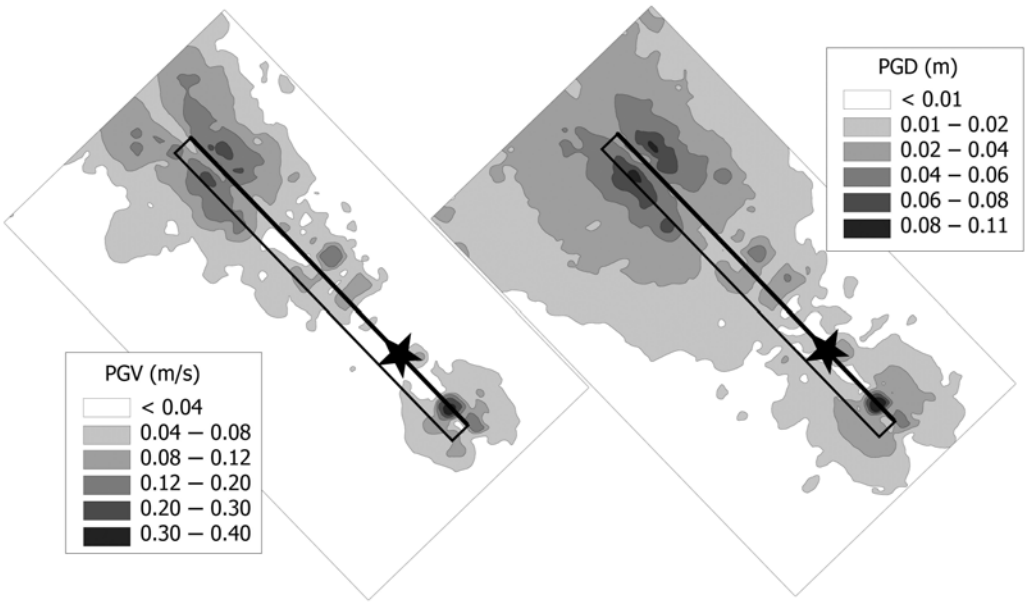

Figure 14. The ground surface distribution of (left) PGVs and (right) PGDs as obtained from the slip model of Liu *et al.* (2006). The black line and the black rectangle represent the fault segment and the dipping direction of the fault, and the black star represents the epicenter.

the slip model of Liu *et al.* (2006) and using the entire simulation grid, is presented in Figure 14. Simulated SAs at $T = 3.0$ are compared with ShakeMap data of the Parkfield earthquake (see Data and Resources) in Figure 15. Ground-motion distributions obtained from simulated and recorded data based on station locations only (Fig. 13) reveal a narrowband of mean ground motion close to the epicenter. This is also reflected in Figure 14, whereas in the ShakeMap application, which is predominantly based on ground-motion prediction equations using functions of fault distance models, a larger band of high peak values is evident around the fault. Otherwise, considering that the ShakeMap also incorporated soil amplification effects at shallow depths, the agreement between the two models and distribution of the peaks is quite satisfactory. The Gold Hill array, situated very close to the epicenter, captured the ground-motion distribution extremely well. The low values of PGV and PGD around the epicenter computed by the numerical simulations are realistic, as the same values are observed in the recordings. Low-wave amplitudes near the epicenter are a consequence

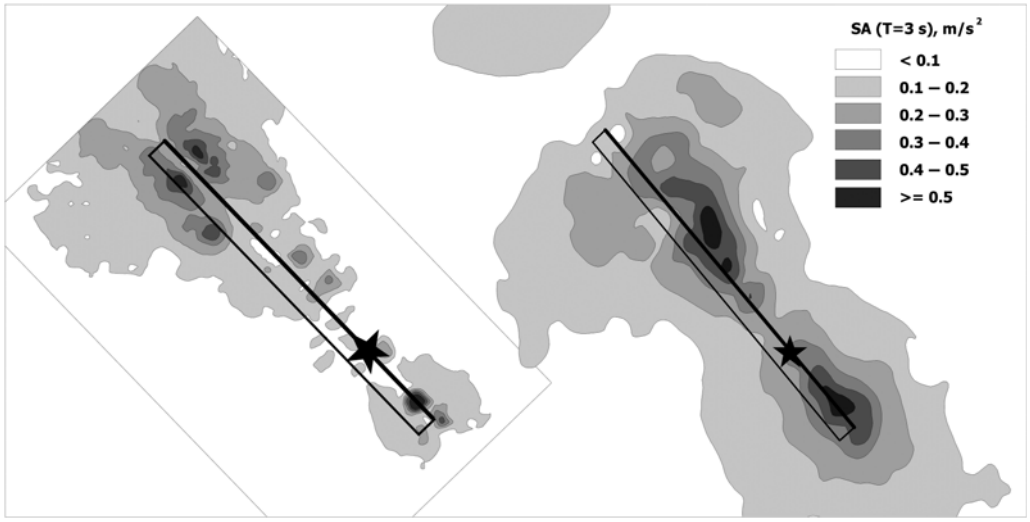

Figure 15. Comparison of the ground surface distribution of SA ($T = 3.0$ s) obtained from (left) simulated wavefield and (right) from California Integrated Seismic Network (CISN) ShakeMap.

of the low values of slip that characterize the rupture initiation of the Parkfield earthquake. As shown by Twardzik *et al.* (2012), this is a robust feature of the slip distribution. Among the 12 models retained by these authors, only three had a significant slip near the hypocenter.

Shakal *et al.* (2006) showed that the observed PGVs from the Parkfield earthquake follow the common ground-motion prediction equations fairly well except within 10 km fault distance. The spread in the PGVs at distances less than 10 km was a factor of about 10. In Figure 16, we compared the synthetic and observed PGVs within 20 km of the fault with the ground-motion prediction model of Campbell and Bozorgnia (2008; hereafter referred to as CB2008) for a strike-slip M_w 6.0 earthquake and bedrock conditions). We plot FN and FP components of both synthetic and recorded ground motion. The observed PGVs shown in Figure 16 are filtered between 0.1 and 1.0 Hz to provide a common basis of comparison with their simulated counterparts. They therefore are not expected to conform to CB2008 in a perfect sense and to be significantly lower. On average, the recorded, filtered PGVs are lower than the mean PGVs by a factor of 4; the mean PGVs have been shown to conform well with the unfiltered recorded PGVs by Shakal *et al.* (2006). FP and FN components of the synthetic PGVs share the same trend and coverage with recorded PGVs. We can make similar observations and comments for the fit of observed and synthetic PGDs. Their spread around the mean and ± 1 standard deviation PGDs estimated by CB2008 is slightly better than the spread of PGVs. In the same figure, we also plot 5% damped SAs at $T = 2.0$ and 5.0 s of synthetic and observed ground motion and compare them with CB2008. There is a very reasonable fit between the synthetics and observations. Both recorded and synthetic FN SAs are larger than the FP SAs.

Figure 17 presents the comparison of synthetic SAs (for the periods of 1.5, 2.0, 3.0, 4.0, 5.0, and 10.0 s), PGVs, and PGDs with CB2008. In each case, we plot the mean ground-motion value, computed by the geometric mean of the two components. In the figure, we also distinguish between the simulation points in the forward directivity region and in the no-directivity region. The directivity region covers all simulation points located within 45° of the fault strike on both sides of the epicenter. Remaining points in the simulation grid are considered to be in the no-directivity region. Evaluating all synthetics together (i.e. without making any differentiation with respect to directivity), we observe a very reasonable match of the SAs with CB2008 at all periods in terms of their slope and spread. Synthetic PGVs and PGDs are lower than those estimated by CB2008, yet their slope is similar to the drop-off of the CB2008 estimations. This is an expected outcome, as already shown in Figure 16 and discussed in the previous paragraph.

A more interesting point of discussion, is the strikingly different behavior of all engineering parameters with respect to directivity. With that in mind, we look at these parameters in the first 20 km of the fault. The first observation we make is that, particularly at fault distances less than 10 km, the points in the directivity region experience ground-motion amplitudes larger than those in the no-directivity region by a factor of 2–4. The second observation is that the ground-motion amplitudes practically do not change within 10 km of the fault and remain the same in the no-directivity region. They start to drop very slightly between 10 and 20 km. The drop that we observe in ground-motion amplitudes in the directivity region is larger than that observed in the no-directivity region.

Directivity Considerations

The distinct separation between the mean ground-motion parameters in the directivity and no-directivity regions that we observe in Figure 17 suggests that modification of the ground-motion prediction equations for directivity may be

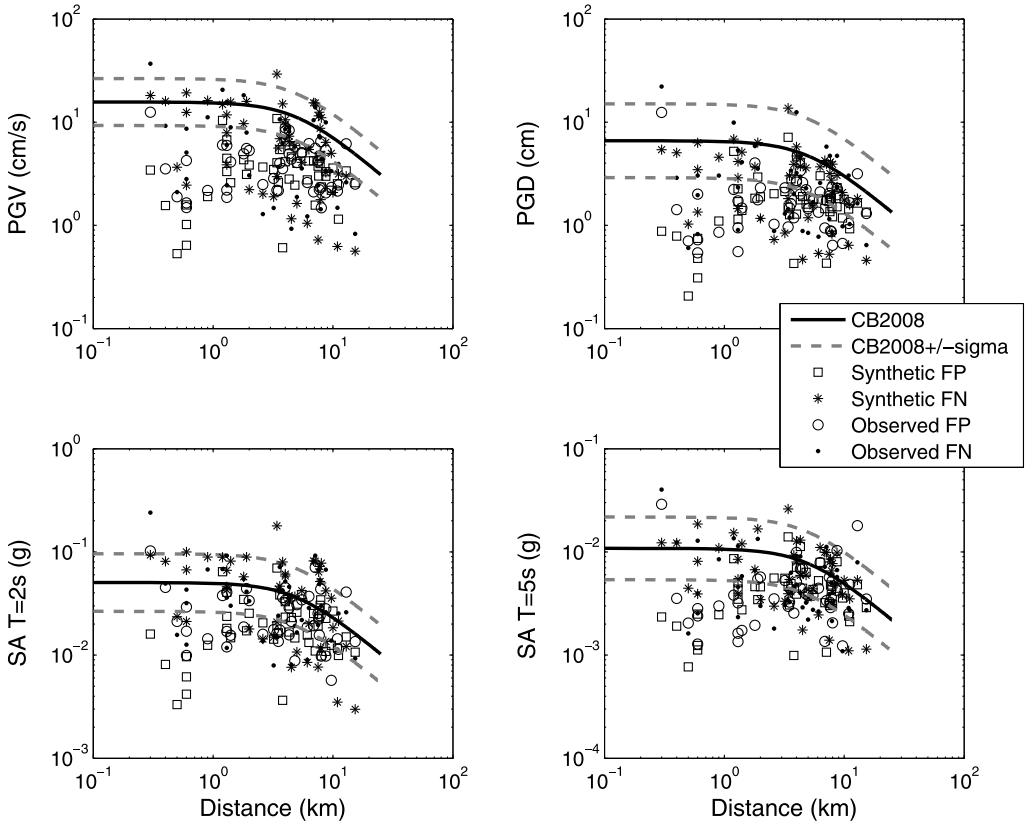

Figure 16. Comparison of simulated and recorded PGVs, PGDs, and SAs ($T = 2.0$ and 5.0 s) in FN and FP directions with CB2008. Recorded ground motions at the observation points are filtered between 0.1 and 1.0 Hz and corrected for engineering bedrock conditions to enable a comparison with simulations. Site correction is carried out after the coefficients provided by Liu *et al.* (2006).

feasible. The model of Somerville *et al.* (1997), later modified by Abrahamson (2000), involves a geometrical expression of the site with respect to the epicenter. It is widely used for the prediction of amplification of ground-motion parameters. Later on, Spudich and Chiou (2008) and Rowshandel (2010) proposed means for the modification of the Next Generation Attenuation (NGA) models for directivity. Spudich and Chiou (2008) relied on theoretical modeling in developing their model. Rowshandel (2010) used data from individual earthquakes. Yet the two models kept elements for the definition of the site location with respect to the fault in their mathematical expressions. Based on our simulation results, however, we hypothesize that a simpler model based on similar parameters adopted for the NGA models can be developed. This is only a hypothesis at this stage but is worth exploring if supported by further simulations.

We study the variation of synthetic FN and FP components with distance in Figure 18. The drop with distance that we observe in the FP components is captured very well by CB2008 for all SAs, as well as for PGVs and PGDs. The FN components are on average larger than FP components and sustain the same amplitude in the first 7 km. After 7 km distance, the FN component amplitudes start to drop off at a larger rate than FP components. Generally speaking the match between synthetic SAs at different periods and levels estimated by CB2008 is very satisfactory. The match between synthetic PGVs and PGDs and those estimated by CB2008 is less good, which is to be attributed to filtering applied to the simulations.

There have been attempts to factorize the FN component of ground motion in the near field with respect to mean ground motion. Particularly, the model by Somerville *et al.* (1997) is widely used by researchers and practitioners alike to modify the design spectrum for near-fault conditions. Using the same approach as Somerville *et al.* (1997), we look at the ratio of FN to mean SAs and plot them for periods of 1.5, 2.0, 2.5, 3, 4, and 5 s in Figure 19, where we plot the spatial variation of this ratio in our 30 km × 50 km simulation grid. There is practically an indistinguishable difference between the contour shapes and values associated with different periods. The region with ratios larger than 1 is within 45° of the fault strike on both sides of the epicenter. The ratio varies between 1 and 2 in this region. It reaches a maximum of 2 in a very narrow zone along fault strike for all periods. There is a narrow rectangular region near the epicenter that is about 2 km wide and about 10 km long along the fault strike. The ratios in this region are larger than one. Immediately outside this rectangular shape, we enter into a region where the mean SAs are larger than the SAs in the FN direction. Although these observations are valid for the case of the

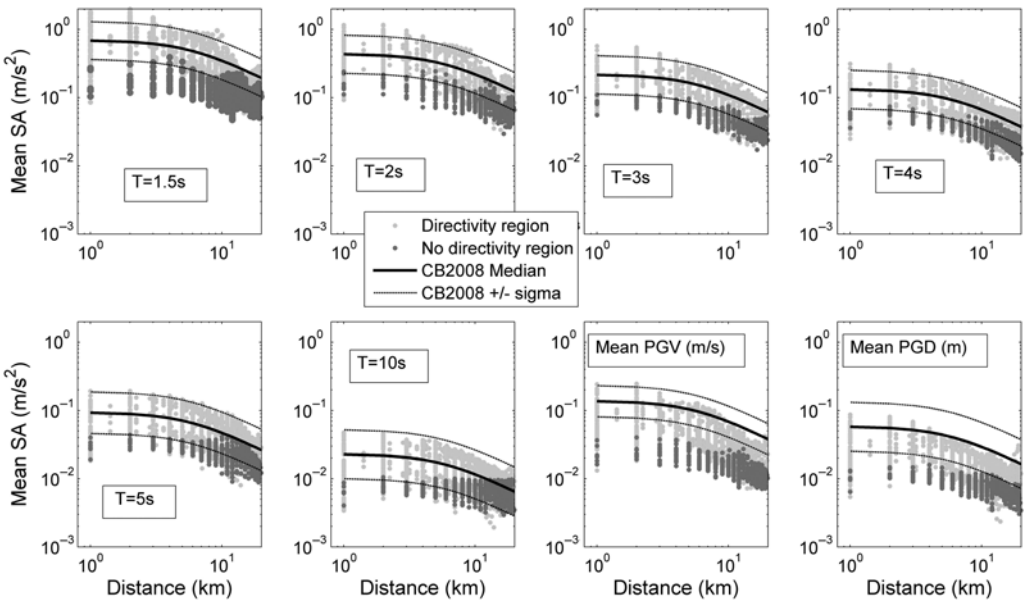

Figure 17. Comparison of synthetic mean 5% damped SAs for the periods of 1.5, 2.0, 3.0, 4.0, 5.0, and 10.0 s and of synthetic mean PGVs and PGDs with CB2008. Simulation points are separated as being in the directivity and no-directivity regions. The directivity region covers all simulation points located within 45° of the fault strike on both sides of the epicenter. The no-directivity region includes all the simulation points remaining outside the directivity region. Mean ground motion is computed as the geometric mean of fault-normal and fault-parallel components.

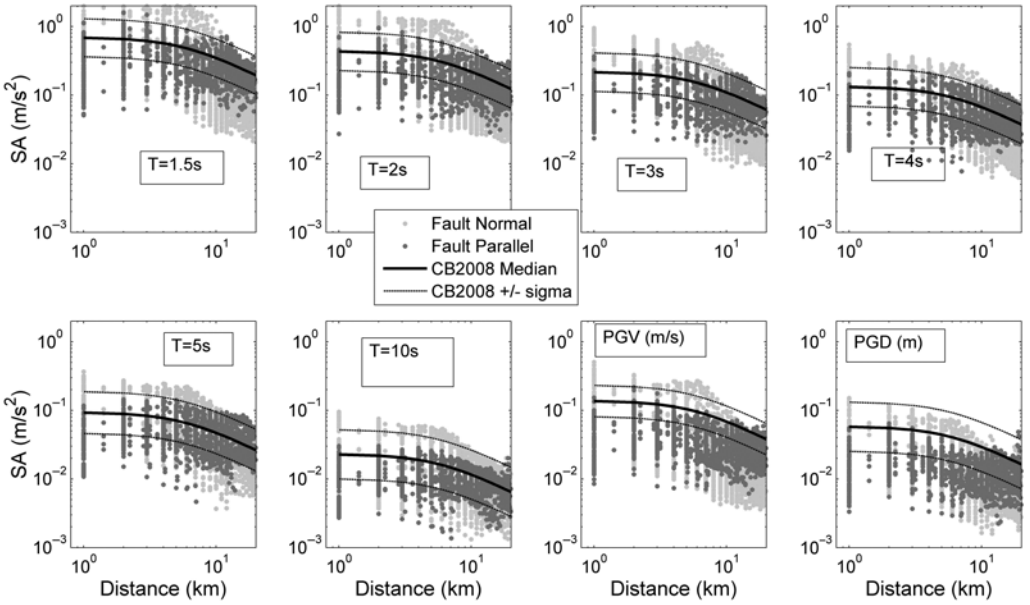

Figure 18. Comparison of synthetic 5% damped fault-normal and fault-parallel SAs for the periods of 1.5, 2.0, 3.0, 4.0, 5.0, and 10.0 s and of synthetic fault-normal and fault-parallel PGVs and PGDs with CB2008.

Parkfield earthquake, they suggest that a simpler model may be developed that is independent of period, can be expressed schematically, and has factors of maximum 2.

As shown in Figure 20, there is a distinct difference between the synthetic FN/FP ratios in the directivity and no-directivity regions. They are considerably larger in the directivity region and almost always greater than 1 up until about 7 km fault distance. In this distance range, they reach values of about 10 for all the parameters we investigate (SA, PGV, PGD). After 7 km there is a rapid drop, which reaches values of the order of 0.5 for all parameters. In the no-directivity region, until a fault distance of 10 km, FN/FP ratios drop slowly. After 10 km, however, there is a region between 10 and 20 km fault distance in which FN/FP ratio either starts

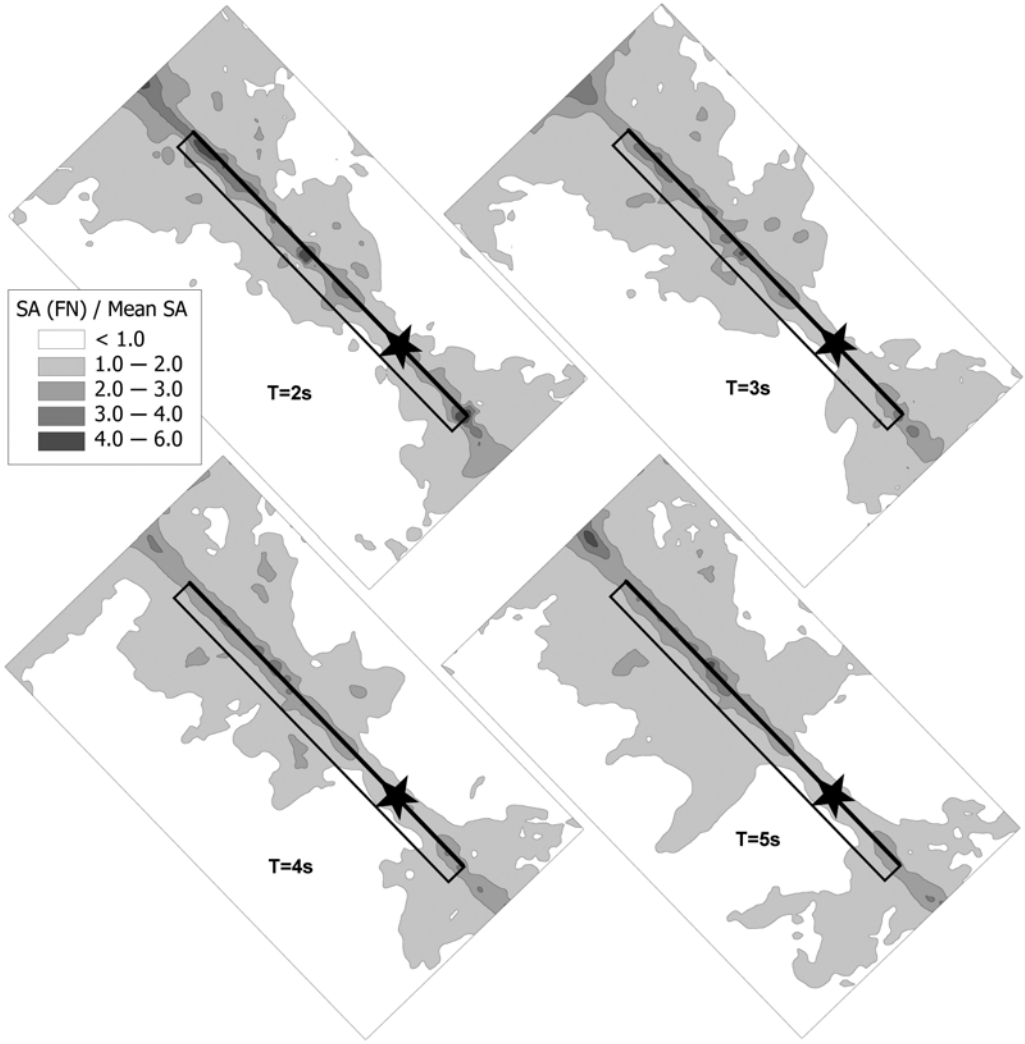

Figure 19. Ratio of FN/mean SA obtained for the 2004 Parkfield earthquake (slip model of Liu *et al.*, 2006).

to increase (SA 1.5, 2.0, 5, 10 s) or remains the same (SA 3.0, 4.0 s, PGV and PGD). It can be said that no clear difference exists between SAs of different periods, PGVs, and PGDs in terms of FN/FP values, their spread, and attenuation. In the same figure, we plot the recorded PGVs and PGDs separated with respect to directivity and no-directivity region with simulations. The match of simulations with recordings is excellent and supports the validity of our interpretations.

Spatial Variability

The spatial variability of simulated PGVs is analyzed using the procedure of Boore *et al.* (2003). Figure 21 compares the spatial variability of recorded and simulated PGVs with the model suggested by Boore *et al.* (2003). When populating the data, the distances are calculated between all possible station pairs in a data set and sorted in increasing order. The station pairs are then grouped into bins according to their interstation distances, with 15 station pairs per bin and interstation spacings of up to 10 km. The mean station spacing of the pairs in each bin is computed. For each pair of a bin, the difference between the logarithms of the PGVs is obtained, and the standard deviations are computed for each bin. In Figure 21, we plot the standard deviations of two types of recorded PGV, with the PGV as recorded by the stations (indicated by diamonds) and the PGV obtained after low-pass filtering at 1 Hz (indicated by squares). Their comparison with the Boore *et al.* (2003) model indicates that filtered and nonfiltered PGVs are equally eligible for use, because their fits with the model are very similar to each other. When we add the standard deviations calculated using simulated PGVs, which are filtered at 1 Hz, to Figure 21, we make two observations. The first observation is the similarity of the standard deviations of filtered PGVs (shown by squares) and simulated PGVs (indicated by triangles). The second observation is the closeness of the fit between the standard deviations of simulated PGVs with the Boore *et al.* (2003) model. This implies that ground-motion parameters estimated by simulations are sufficiently good for use in developing engineering models of spatial variability.

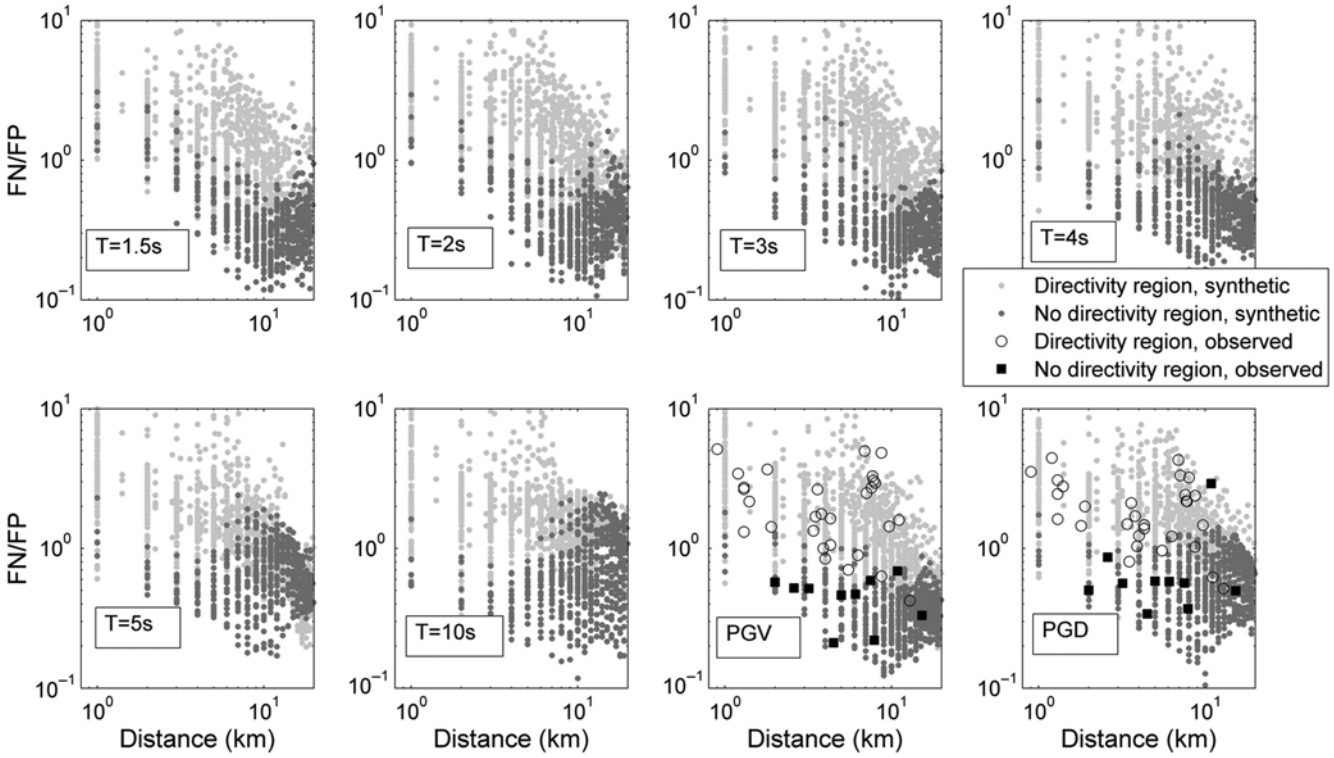

Figure 20. Ratios of FN/FP synthetics for PGV and PGD, separated with respect to whether they are located in the directivity or no-directivity regions (see Fig. 17 for the definition of directivity and no-directivity regions). Recorded PGVs and PGDs, separated according to being in directivity and no-directivity regions, are also shown.

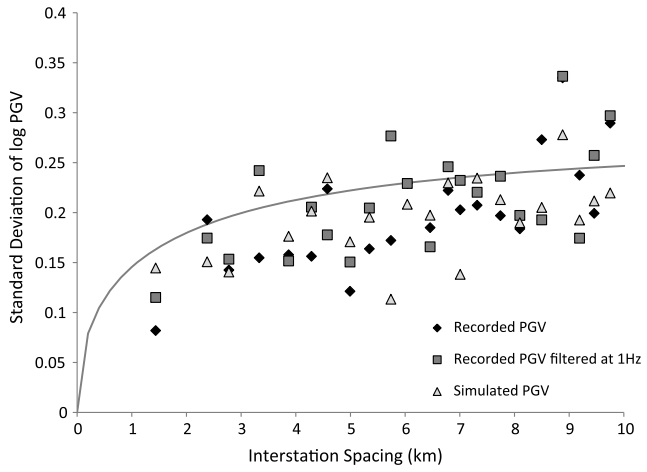

Figure 21. Standard deviation of the difference of the logs of the PGV for all station pairs and for PGVs versus interstation spacing for the Parkfield earthquake. The stations are the ones used for the simulation. The solid line represents the model by Boore *et al.* (2003).

Conclusions

From an overall examination of the stations' recorded and simulated time histories, as well as the modal bias results, we can conclude the following.

- The preferred kinematic model, that of Liu *et al.* (2006), fits observations very well except for stations situated very close to the fault, where fault-trapped waves are dominant.
- Goodness of fit is very sensitive to the slip model used, implying that seismic records contain significant information about slip distribution.
- *S*-wave radiation from the fault plane in the forward-directivity region dominates the goodness of fit of the simulations, because the FN components are more satisfactorily simulated than the FP components in that region, where the slip distribution from the entire rupture plane contributes to the ground motion.
- FP components are best simulated close to the epicentral region, as evidenced by the simulations of the Gold Hill array (which passes through the epicenter), because in that region radiation from only one asperity dominates the ground motion.
- Simulation is generally less satisfactory in the immediate vicinity of the fault where the fault-trapped waves dominate the ground motions.
- Simulation results are generally more successful for the stations located on the eastern side of the fault than those on the western side. This is probably due to the way seismic moment is handled in kinematic inversions. Because the kinematic models are defined by the slip and slip-rate distribution, the moment rate on either side of the fault will be different if the rigidity changes across the fault.

- Simulation of the vertical components can be considered satisfactory given the fact that very low or even no weights were assigned to them during the inversion process.
- Improvement of the goodness of fit was achieved through modifications of various parameters such as slip model, source time function, rise time, and crustal velocity structure. It should, however, be noted that the improvement is mostly achieved in the frequency range higher than 0.4 Hz. Below that level all models yield comparable results.

Comparison of engineering parameters such as PGVs, PGDs, and SAs estimated from simulated and recorded ground motion is important because it provides a basis for the evaluation of the suitability of simulations as a supplement and/or replacement for ground-motion recordings and for ground-motion models. The following are our conclusions drawn from analyses and comparisons presented in the article.

- Recorded and simulated PGVs in FN and FP directions for velocities less than about 6 cm/s are very similar to each other. For velocities larger than 6 cm/s, FP PGVs are overestimated by the simulations. The overestimation, however, remains less than 2. An even better fit is found between recorded and simulated PGDs in FN and FP directions, as well as between the two 5.0 s SAs.
- ShakeMaps produced with the help of simulations instead of ground-motion prediction equations may become common in the near future.
- There is a very reasonable match of the synthetic SAs with CB2008 at periods of 1.5, 2.0, 3.0, 4.0, 5.0, and 10.0 s in terms of their slope and spread. Synthetic PGVs and PGDs are lower than those estimated by CB2008, yet their slope is similar to the drop-off of the CB2008 estimations.
- At fault distances less than 10 km, the points in the directivity region experience ground-motion amplitudes (PGVs, PGDs, SAs) larger than those in the no-directivity region by a factor of 2–4.
- Ground-motion amplitudes practically do not change within 10 km of the fault and remain the same in the no-directivity region. They start to drop very slightly between 10 and 20 km. The drop that we observe in ground-motion amplitudes in the directivity region is larger than that observed in the no-directivity region.
- If supported by further simulations, it appears that a simple model based on modification of the ground-motion prediction equations for directivity can be developed.
- The distance dependence of FP SAs, PGVs, and PGDs is captured very well by CB2008. The FN components are on average larger than FP components in the first 7 km. At greater distances, their amplitudes start to drop off at a larger rate than FP components.
- Current directivity models factorize the FN component of ground motion in the near field with respect to mean ground motion represented in design spectra. The spatial distribution of the ratio of FN to mean synthetic SAs at periods between 1.5 and 5 s results in practically no difference between the contour shapes and values associated with different periods. Although valid for the case of the Parkfield earthquake, they suggest that a simpler model may be developed that is independent of period, can be expressed schematically, and has factors of maximum 2.
- Synthetic FN/FP ratios are considerably larger in the directivity region and almost always greater than 1 up until about 7 km fault distance. In this distance range, they reach values of about 10 for all parameters investigated (SA, PGV, PGD). After 7 km there is a rapid drop, which reaches values in the order of 0.5 for all parameters. In the no-directivity region, until a fault distance of 10 km, FN/FP ratios drop slowly. No clear difference exists between SAs of different periods, PGVs and PGDs in terms of FN/FP values, or their spread and attenuation. The match of simulations with recordings is excellent and supports these interpretations.
- Ground-motion parameters associated with low-frequency motion such as PGV, PGD, and SAs at long periods estimated by simulations are sufficiently good for use in developing engineering models of spatial variability.

Data and Resources

The COSMOS Virtual Data Center was searched using http://strongmotioncenter.org/vdc/scripts/earthquakes.plx (last accessed on August 2014). ShakeMap data of the 2004 Parkfield earthquake were obtained from http://www.cisn.org/shakemap/nc/shake/51147892/products.html (last accessed on August 2014). The Ji (2004) source model was obtained from "Slip History of the 2004 (M_w 5.9) Parkfield Earthquake (Single-Plane Model)," available at http://www.tectonics.caltech.edu/slip_history/2004_ca/parkfield2.html (last accessed on August 2014).

Acknowledgments

This work was partially supported by TUBITAK Project Number 103I050 in Turkey. In France, partial support was provided through Grant ANR-2011-BS56-017 of Agence Nationale de la Recherche in France. Both institutions are gratefully acknowledged. We also thank Associate Editor Hiroshi Kawase, and the anonymous reviewers for their constructive comments that helped us to improve the article.

References

Abrahamson, N. A. (2000). Effects of rupture directivity on probabilistic seismic hazard analysis, *Proc. Sixth International Conference on Seismic Zonation*, Palm Springs, California, 12–15 November 2000, Earthquake Engineering Research Institute (EERI).

Bakun, W. H., and A. G. Lindh (1985). The Parkfield, California, earthquake prediction experiment, *Science* **229,** 619–624.

Bakun, W. H., and T. V. McEvilly (1979). Earthquakes near Parkfield, California: Comparing the 1934 and 1966 sequences, *Science* **205,** 1375–1377.

Bakun, W. H., B. Aagaard, B. Dost, W. L. Ellsworth, J. L. Hardebeck, R. A. Harris, C. Ji, M. J. S. Johnston, J. Langbein, J. J. Lienkaemper, *et al.* (2005). Implications for prediction and hazard assessment from the 2004 Parkfield earthquake, *Nature* **437,** 969–974.

Boore, D. M., J. F. Gibbs, W. B. Joyner, J. C. Tinsley, and D. J. Ponti (2003). Estimated ground motion from the 1994 Northridge, California, earth-

quake at the site of the interstate 10 and La Cienega Boulevard bridge collapse, west Los Angeles, California, *Bull. Seismol. Soc. Am.* **93,** 2737–2751.

Borcherdt, R. D., M. Johnston, G. Glassmoyer, and C. Dietel (2006). Recordings of the Parkfield 2004 earthquake on the GEOS array: Implications for earthquake precursors, fault rupture, and coseismic strain changes, *Bull. Seismol. Soc. Am.* **96,** no. 4B, S73–S89.

Brocher, T. M. (2005). Empirical relations between elastic wavespeeds and density in the Earth's crust, *Bull. Seismol. Soc. Am.* **95,** no. 6, 2081–2092.

Brune, J. N. (1970). Tectonic stress and the spectra of seismic shear waves from earthquakes, *J. Geophys. Res.* **75,** 4997–5009.

Campbell, K. W., and Y. Bozorgnia (2008). NGA ground motion model for the geometric mean horizontal component of PGA, PGV, PGD and 5% damped linear elastic response spectra for periods ranging from 0.01 to 10 s, *Earthq. Spectra* **24,** no. 1, 139–171.

Courant, R., K. Friedrichs, and H. Lewy (1928). Über die partiellen Differenzengleichungen der mathematischen Physik, *Mathematische Annalen* **100,** no. 1, 32–74 (in German).

Dreger, D. S., L. Gee, P. Lombard, M. H. Murray, and B. Romanowicz (2005). Rapid finite-source analysis and near-fault strong ground motions: Application to the 2003 M_w 6.5 San Simeon and 2004 M_w 6.0 Parkfield earthquakes, *Seismol. Res. Lett.* **76,** no. 1, 40–48.

Gallovič, F., M. Kaser, J. Burjánek, and C. Papaioannou (2010). Three-dimensional modeling of near-fault ground motions with nonplanar rupture models and topography: Case of the 2004 Parkfield earthquake, *J. Geophys. Res.* **115,** no. B03308, doi: 10.1029/2008JB006171.

Graves, R. (1996). Simulating seismic wave propagation in 3D elastic media using staggered-grid finite differences, *Bull. Seismol. Soc. Am.* **86,** no. 4, 1091–1106.

Ji, C., K. Choi, N. King, K. M. Larson, and K. W. Hudnut (2004). Co-seismic slip history and early afterslip of the 2004 Parkfield earthquake, *Eos Trans. AGU* **85,** no. 47 (Fall Meet. Suppl.), Abstract S53D-04.

Levander, A. R. (1988). Fourth-order finite-difference *P-SV* seismograms, *Geophysics* **53,** no. 11, 1425–1436.

Liu, P., S. Custodio, and R. J. Archuleta (2006). Kinematic inversion of the 2004 M 6.0 Parkfield earthquake including an approximation to site effects, *Bull. Seismol. Soc. Am.* **96,** no. 4B, S143–S158.

Ma, S., S. Custodio, R. J. Archuleta, and P. Liu (2008). Dynamic modeling of the 2004 M_w 6.0 Parkfield, California earthquake, *J. Geophys. Res.* **113,** no. B02301, doi: 10.1029/2007JB005216.

Madariaga, R. (1976). Dynamics of an expending circular fault, *Bull. Seismol. Soc. Am.* **66,** no. 3, 639–666.

Madariaga, R., K. B. Olsen, and R. Archuleta (1998). Modeling dynamic rupture in a 3D earthquake fault model, *Bull. Seismol. Soc. Am.* **88,** no. 5, 1182–1197.

McJunkin, R. D., and A. F. Shakal (1983). The Parkfield Strong-Motion Array, California, *Geology* **36,** 27–34.

Mena, B., E. Durukal, and M. Erdik (2006). Effectiveness of hybrid Green's function method in the simulation of near-field strong motion: An application to the 2004 Parkfield Earthquake, *Bull. Seismol. Soc. Am.* **96,** no. 4B, S183–S205.

Miyatake, T. (1980). Numerical simulations of earthquake source process by a three-dimensional crack model. Part I. Rupture process, *J Phys. Earth* **28,** 565–598.

Moczo, P., J. Kristek, and M. Galis (2014). *The Finite-Difference Modelling of Earthquake Motions Waves and Ruptures*, Cambridge University Press, Cambridge, United Kingdom.

Olsen, K. B., and R. J. Archuleta (1996). Three-dimensional simulation of earthquakes on the Los Angeles fault system, *Bull. Seismol. Soc. Am.* **86,** 575–596.

Olsen, K. B., R. J. Archuleta, and J. R. Matarese (1995). Three-dimensional simulation of a magnitude 7.75 earthquake on the San Andreas fault, *Science* **270,** 1628–1632.

Pitarka, A., and K. Irikura (1996). Modeling 3-D surface topography by finite-difference method: The Kobe JMA station site case study, *Geophys. Res. Lett.* **23,** 2723–2732.

Rowshandel, B. (2010). Directivity correction for the Next Generation Attenuation (NGA) relations, *Earthq. Spectra* **26,** no. 2, 525–559.

Shakal, A., V. Graizer, M. Huang, R. Borcherdt, H. Haddadi, K. Lin, C. Stephens, and P. Roffers (2005). Preliminary analysis of strong-motion recordings from the 28 September 2004 Parkfield, California earthquake, *Seismol. Res. Lett.* **76,** 27–39.

Shakal, A., H. Haddadi, V. Graizer, K. Lin, and M. Huang (2006). Some key features of the strong-motion data from the **M** 6.0 Parkfield, California, earthquake of 28 September 2004, *Bull. Seismol. Soc. Am.* **96,** no. 4B, S90–S118.

Somerville, P. G., N. F. Smith, R. W. Graves, and N. A. Abrahamson (1997). Modification of empirical strong motion attenuation relations to include the amplitude and duration effects of rupture directivity, *Seismol. Res. Lett.* **68,** 199–222.

Spudich, P. B., and B. S.-J. Chiou (2008). Directivity in NGA earthquake ground motions: Analysis using isochrone theory, *Earthq. Spectra* **24,** 279–298.

Thurber, C., H. Zhang, F. Waldhauser, J. Hardebeck, A. Michaels, and D. Eberhart-Phillips (2006). Three-dimensional compressional wavespeed model, earthquake relocations, and focal mechanisms for the Parkfield, California region, *Bull. Seismol. Soc. Am.* **96,** no. 4B, S38–S49.

Twardzik, C., S. Das, and R. Madariaga (2014). Inversion for the physical parameters that control the source dynamics of the 2004 Parkfield earthquake, *J. Geophys. Res.* **119,** doi: 10.1002/2014JB011238.

Twardzik, C., R. Madariaga, S. Das, and S. Custodio (2012). Robust features of the source process for the 2004 Parkfield, California, earthquake from strong-motion seismograms, *Geophys. J. Int.* **191,** 1245–1254.

Virieux, J. (1986). *P-SV* wave-propagation in heterogeneous media: Velocity-stress finite-difference method, *Geophysics* **51,** 889–901.

Boğaziçi University
Kandilli Observatory and Earthquake Research Institute
Çengelköy, 34684 İstanbul, Turkey
karin@boun.edu.tr
(K.Ş., E.Ç.)

Ecole Normale Superieure
24 rue Lhomond
75230 Paris Cedex 05 France
madariag@geologie.ens.fr
(R.M.)

Manuscript received 29 August 2014;
Published Online 5 May 2015